Bulletin of Geophysics and Oceanography
DOI 10.4430/bgo00507

From linear model to machine learning algorithms: performance analysis of horizontal GNSS velocities of the coastal southern Scandinavia

M. Eren

Department of Geomatic Engineering, Yildiz Technical University, Istanbul, Turkey

(Received: 29 March 2025; accepted: 22 September 2025; published online: 6 March 2026)

ABSTRACT Accurate determination of the Global Navigation Satellite System (GNSS) velocities plays a very important role in describing the tectonic process, crustal deformation, and many other geodetic applications. This study aims to compare the efficiency of linear regression (LR) models with machine learning (ML) algorithms, such as Decision Trees (DTs), Random Forest (RF), and Gaussian process regression (GPR), in estimating horizontal GNSS velocities. In this context, data from 20 Continuously Operating Reference Stations (CORSs) on the southern Scandinavian peninsula were used. The findings show that the RF and GPR ML techniques perform much better than the LR models, giving an R^2, higher than 0.94 while having a lower root-mean-square error and mean absolute error. The velocities estimated with the help of DTs are comparable to LR results and show that DTs are applicable in GNSS time series velocity estimation. However, in this study, it is seen that DTs improve the results even further in capturing nonlinear patterns compared to the LR-based approach. This study improves the accuracy of horizontal velocity estimates based on GNSS time series data, considering the limitations of classical models, and highlights the potential success of ML techniques in GNSS velocity estimation. These findings can provide a critical framework for improving geophysical and geodetic analyses in infrastructure planning, crustal movement monitoring, and disaster risk reduction.

Key words: GNSS velocity estimation, machine learning, GIPSY-X, land motion, tectonics, crustal dynamics, campaign GNSS data.

1. Introduction

The estimation of horizontal velocities at Global Navigation Satellite System (GNSS) stations is important for applications ranging from tectonic studies to infrastructure development. GNSS data, an important tool for establishing terrestrial reference frames, are widely used to study Earth kinematics (Altamimi *et al.*, 2016; Sosnica *et al.*, 2018). Velocity estimation of GNSS stations is based on classical methods, especially linear regression (LR) techniques. For example, Alif *et al.* (2023) showed that present-day velocities in western Sumatra were calculated using LR and were consistent for all GNSS sites, which is compatible with the tectonic subduction dynamics of the region (Erkoç and Doğan, 2023). However, Zhang *et al.* (2023) pointed out the fact that, because this methodology only uses the linear interpolation approach for the GNSS velocity field, it usually lacks detail in the area with sparse distribution of the station.

The machine learning (ML) algorithms identify complicated nonlinear relationships that might exist in the GNSS data, unlike in classical approaches like kriging and least-squares fitting, which intrinsically assume linearity (Li *et al.,* 2023). This provides particular value in conditions of sparse station coverage where considerable gain in accuracy within velocity estimation is achieved through the usage of ML. For example, Quan *et al.* (2018) showed that ML methods improved positioning accuracy in challenging conditions, while Granat *et al.* (2021) showed how cluster analysis captured long-term velocity trends and co-seismic offsets in California. In line with this, Yanez-Cuadra *et al.* (2023) applied unsupervised ML methods to GNSS velocities along the Chilean trench, revealing crustal motion that was not captured by traditional methods. Research by Li *et al.* (2023) further illustrated the ability of ML techniques to improve data reliability by filtering out erroneous measurements. In addition to improving accuracy, ML methods streamline the entire process of data analysis, reducing the possibility of human error and increasing efficiency. Heflin *et al.* (2020) developed automated tools for extracting position, velocity, and seasonal effects from daily GNSS measurements, which have explained complex deformation patterns. Automation tools allow the researcher to invest more time in interpreting the results rather than manually processing data.

ML algorithms have a different structure than classical methods, such as kriging and least squares fitting, which rely on the assumption of linearity. ML methods can provide estimates that are more reliable than traditional least square methods (Gao *et al.*, 2022). Despite the advantages, integrating ML techniques into GNSS applications presents a number of challenges. The complexity of GNSS data causes poor performance of ML models depending on the signal quality affected by environmental factors and the quality of the training data. For example, multipath effects reduce positioning accuracy and make velocity estimation difficult (Kamatham, 2018). Different ML methods have been proposed to capture multipath effects and mitigate their effects. However, the effectiveness of these methods is directly related to the quality of the training dataset (Quan *et al.,* 2018; Wang *et al.*, 2022). Moreover, advanced techniques, such as deep learning, are computationally intensive and time-consuming for training data, which makes them difficult to use in dynamic environments where velocity is critical (Agarwal *et al.*, 2023).

Although relatively tectonically stable, the southern Scandinavian peninsula faces major coastal dynamics due to sea level rise, thus increasing the risks of inundation and erosion (Peng *et al.*, 2021). Furthermore, the occurrence of small tectonic movements in the region, together with the proximity to low-lying coastal areas, underlines the need for sensitive monitoring of crustal movements. This is crucial for understanding and mitigating the impacts of environmental changes caused by sea level rise. GNSS-based velocity data provides valuable information for monitoring coastal processes and sea level changes (Peng *et al.*, 2021). Thus, it plays a significant role in decision-making processes. As stated by Okazaki *et al.* (2021), networks of the CORSs provide a significant contribution in monitoring ongoing deformation.

This paper represents the performance comparison of the classical linear models and state-of-the-art ML algorithms regarding regional velocity estimates from GNSS stations distributed along the coastline of the southern Scandinavian peninsula. A network of 20 GNSS stations have been analysed with the use of LR, Decision Tree (DT), Random Forest (RF), and Gaussian process regression (GPR). Continuously operating GNSS [continuously Operating Reference Station (CORS)] and campaign measurements were processed using GIPSY-X software. The novelty of this study is the comparison of four different velocity estimation methods for two types of measurements in a comprehensive analysis of GNSS velocity estimation techniques in such context.

2. Materials and methods

2.1. Study area and GNSS stations

The study aims to determine the GNSS horizontal velocities using classic LR, DT, RF, and GPR approaches, and to compare the performance of RF and GPR with that of DT. In the performance comparison process, mean absolute error (MAE) and root-mean-square error (RMSE) criteria were used. In this context, a network of 20 CORSs distributed along the coasts of the southern Scandinavian peninsula region was selected (Fig. 1). The primary reason for selecting the study area is that the average data gap rate is less than one percent (0.76). Another factor is that since 1996 (when the first data were used), there have been no earthquakes that could affect the location of the stations in this region (USGS, n.d.). Earthquakes can complicate the interpretation of GNSS data and lead to difficulties in accurately estimating velocity trends. For example, after the Tohoku-Oki earthquake, velocity vectors in South Korea were reported to change direction and magnitude (Kim *et al.*, 2018).

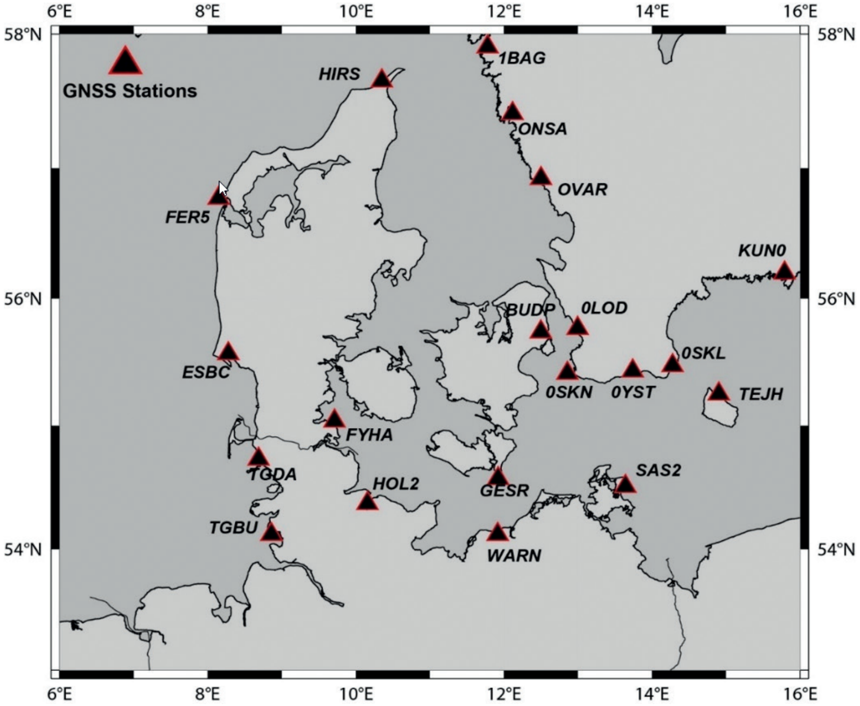

Fig. 1 - Study area.

When examining the earthquakes listed in Table 1, the largest earthquake that occurred between 1996 and 2024 was the 4.4 M_w earthquake. The distance between the epicentre of this earthquake, which, however, was not large, and the nearest station is 55 km. In other words, it was evaluated that the magnitude of this earthquake was small (not large enough to cause offset) and had no effect on the velocities because the epicentre was far from the stations.

Table 1 - List of earthquakes that occurred in the study region between 1996 and 2024.

Date	Latitude (°)	Longitude (°)	Magnitude	Depth (km)
08.07.1998	56.672	7.473	3.3 M_L	10.0
21.07.2001	54.000	12.500	3.5 M_L	10.0
21.10.2001	56.780	7.551	3.5 M_L	10.0
24.11.2004	56.899	11.732	3.0 M_L	10.2
24.11.2004	56.957	11.278	3.1 M_L	15.0
03.02.2005	56.165	11.460	3.0 M_L	0.0
03.02.2005	56.142	11.199	3.0 M_L	0.1
16.12.2008	55.514	13.410	4.3 M_W	10.0
19.02.2010	56.880	7.503	4.4 M_B	10.0
06.08.2012	56.607	12.053	4.2 M_B	9.8
29.07.2015	57.800	11.902	3.4 M_L	13.4
16.09.2018	56.399	8.029	3.8 M_B	10.0

2.2. GNSS data processing

In this study, the processed GNSS data were obtained from the SONEL website (SONEL, n.d.). GNSS data from continuous and campaign-style observations were processed in GIPSY-X version 2.1 software. The data consist of observations from the stations listed in Fig. 2, covering periods exceeding 10 years (9 years for one station only) and with varying levels of data gaps. Continuous GNSS (CORS) data consist of 24-hour observations, while campaign GNSS data are simulated as daily observations taken between 09:00 and 17:00. The data processing and analysis approach of the GIPSY-X software is described in detail below.

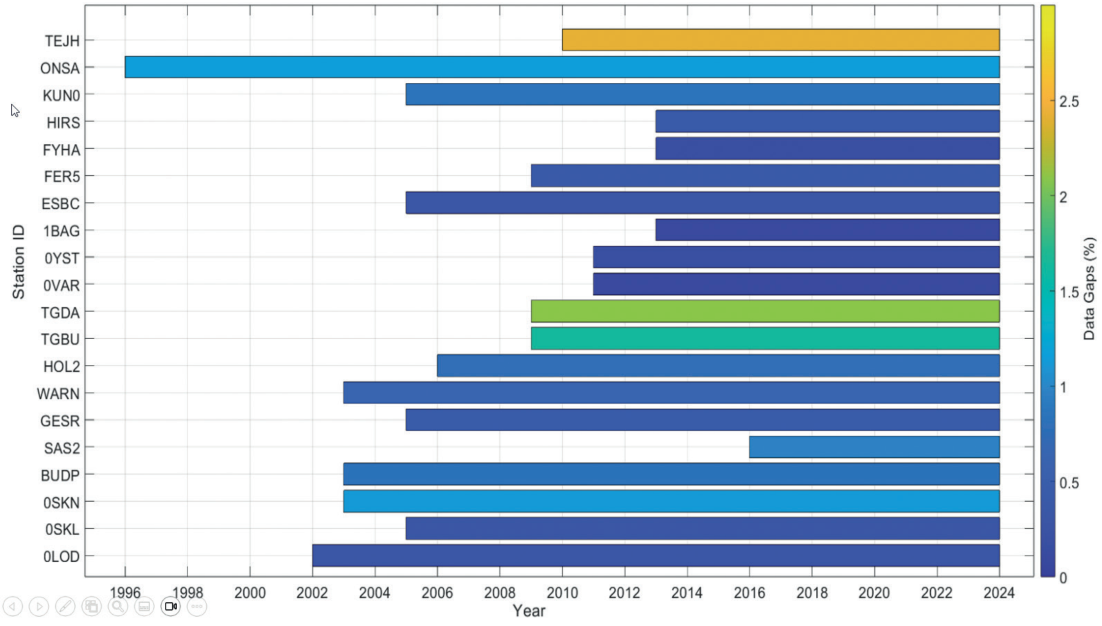

Fig. 2 - Data acquisition times and data gaps for the stations used in the study.

2.2.1. Data quality assessment

The raw GNSS observations were first examined for quality using the GIPSY-X built-in tools. This step included identifying and mitigating multipath effects, data gaps, and cycle slips. Stations with significant gaps require interpolation or exclusion of problematic segments.

2.2.2. Precise point positioning

Using the GIPSY-X precise point positioning approach, GNSS data are processed as follows:

- precise satellite orbit and clock error correction data from the Jet Propulsion Laboratory (JPL). Modelling of atmospheric delay is accomplished using the Global Mapping function to account for tropospheric effects;
- ocean tide loading corrections, using models such as FES2004;
- antenna phase centre corrections based on International GNSS service (IGS) calibration models.

Observation periods and sampling rates are as follows:

CORS data: the processing of CORS data as continuous 24-hour daily observations ensures that daily coordinates are determined with consistent accuracy;

campaign data*:* these are simulated as campaign-style observations taken between 09:00 and 17:00. The times covered during these hours are a balance between keeping the observations accurate and being practical. Additionally, care has been taken to ensure there are no data gaps in the analysis of campaign data. In this context, data from all stations were reviewed, and the 5th, 6th, and 7th days of October were selected;

reference frame realisation: station positions and velocities are estimated in the ITRF2020 reference frame. GIPSY-X has been configured in such a way that it is able to minimise station inconsistencies caused by tectonic movements, thereby ensuring the provision of accurate trend estimates.

2.2.3. Time series analysis

Station coordinates. Daily solutions are utilised to generate time series for each station, thereby facilitating the discernment of vertical and horizontal land movement trends.

Data gaps. For the missing data in GNSS data, the K-nearest neighbour interpolation method was used only because the data gaps did not exceed 5% of the total time series length. Consistent and complete data increases reliability in time series (Zhang *et al.*, 2021). For this study, a time interval was selected that would have no data gaps on consecutive days. Since the data follows a daily and smooth course, the K value of 5 was selected.

Error modelling and estimation. GIPSY-X employs a stochastic error model to account for:

- satellite-specific biases;
- temporal variations in atmospheric conditions;
- station-dependent noise characteristics.

The raw GNSS observations were initially subjected to a quality assessment utilising the GIPSY-X integrated tools. This step comprised the identification and mitigation of multipath effects, data gaps, and cycle slips.

Result integration. Processed coordinates were integrated into a database for subsequent statistical analysis, including trend estimation using ML models in the broader study framework. By employing GIPSY-X for rigorous processing, this study ensures that GNSS-derived insights into vertical and horizontal land motion are both precise and reliable. The combination of continuous and campaign-style data allows for a comprehensive evaluation of the stations over their respective operational periods.

Estimation of GNSS velocities using linear models is a critical area of research, especially in applications that require high precision and reliability. Vu *et al.* (2023) emphasise that LR is an algorithm that can effectively estimate the relationships between dependent and independent variables in GNSS applications and is widely used in analysing time series data. This approach is particularly useful in identifying trends in GNSS measurements that may be affected by various types of noise, including vibration and random noise.

Eq. (1) is typically used to estimate GNSS station velocities with a linear model:

$$P(t) = V \cdot t + P_0 + \epsilon \tag{1}$$

where, $P(t)$ is position of the GNSS station at time t (north, east, and up), V is the velocity in the relevant direction (average movement velocities of the GNSS station), t is the time of the GNSS observation, P_0 is the initial position of the GNSS station at a reference time (e.g. $t = 0$ or an initial observation time), and ε is the random error term accounting for measurement noise and other small variations. In order to evaluate model accuracy, the residual sum of squares (RSS) is calculated as:

$$RSS = \sum_{i=1}^{n}(y_i - \hat{y}_i)^2 \tag{2}$$

where y_i is the observed value, $\hat{y}_i$ is the predicted value, and n is the number of observations.

The model assumes that position $P(t)$ changes linearly over time at a given V. By fitting this linear model to a time series of GNSS observations, the estimated slope represents the station's average velocity, V, in that direction.

Linear models are preferred because of the ease of implementation of the GNSS velocity estimates, simple model setup, and interpretability. When analysing long-term data, GNSS velocity changes can be linearised to obtain accurate results. In addition to traditional LR methodologies, ML techniques are being increasingly used in GNSS velocity estimation. Zhang and Wang (2019) proposed a ML algorithm to improve positioning accuracy during GNSS outages. The use of linear models in GNSS velocity estimation may result in lower accuracy. Furthermore, several studies emphasised that the use of first-order Taylor series approximations classical LR methods may lead to loss of detail (Zhang and Wang, 2019; Erkoç and Doğan, 2024). To overcome this problem, linear models supported by advanced ML-based computational methods can improve GNSS velocity estimation. Recent research on GNSS velocity field estimation has shown a greater focus on RF, GPR, and DT algorithms. The use of these algorithms provides significant advantages over traditional statistical approaches by modelling the complex and nonlinear relationships found in GNSS data. As a result, these models have the potential to increase the accuracy and reliability of velocity estimations.

2.3. Machine learning models

2.3.1. Decision trees

The effectiveness of DTs in GNSS velocity data estimation can be attributed to its provision of a non-parametric approach which is capable of modelling complex and nonlinear relationships in data. The iterative division of the dataset, according to feature values, enables DTs to capture nonlinear relationships in GNSS velocity estimation. This method has been shown to effectively handle heterogeneous data with varying characteristics and noise levels, including Doppler and carrier phase measurements (Angrisano *et al.*, 2024). However, it is imperative to avoid overfitting in the context of large-scale data and high-noise data. Christianti *et al.* (2020) have demonstrated that over-learning can result in the model learning the data noise patterns, thereby weakening its generalisation capacity. In DT regression, the predicted value for an input is determined by the mean of observations within a terminal region *Rm*. The Prediction function is expressed as:

$$SL(t) = \sum_{i=1}^{M} \hat{c}_m \, I(t \in R_m) \tag{3}$$

where $\hat{c}_m$ is the predicted value (mean) in region R_m, R_m is the *m*-th region (leaf node) of the tree, $I(t \in R_m)$ is an indicator function that returns 1 if sample t belongs to region R_m, and 0 otherwise, *M* is the total number of terminal regions (leaves) in the tree.

2.3.2. Random forest

RF, an ensemble learning method, is successful in handling these complexities due to its ability to model nonlinear relationships and reduce overfitting of traditional single DTs (Crocetti *et al.*, 2021). RF can handle high-dimensional data, making it more reliable for GNSS velocity estimation, and can provide insights into feature importance, which is useful for understanding which GNSS measurements contribute the most to velocity estimation (Dittmann *et al.*, 2022). It has a significant disadvantage in decision-making processes due to the interpretability problem (Fantazzini *et al.*, 2021). In RF, the final prediction is the average of predictions from all DTs in the ensemble:

$$\hat{y}(x) = \frac{1}{B} \sum_{b=1}^{B} T_b(x) \tag{4}$$

where $T_b(x)$ is the prediction from the *b*-th DT, *B* is the total number of trees in the forest, *x* is the input feature vector.

2.3.3. Gaussian process regression

GPR is a non-parametric Bayesian regression method that models the relationship between inputs and outputs with the help of kernel functions, and enables accurate predictions even in small datasets (Roushangar and Shahnazi, 2020; Dalmasso *et al.*, 2025). In GNSS applications, GPR estimates position or velocity values while also quantifying uncertainty (Atia *et al.*, 2011). The flexibility of modelling complex and nonlinear relationships without the need for a predefined function makes this method suitable for use in geodetic data analysis (Hewing *et al.*, 2019). Commonly used kernel functions include linear and Radial Basis function (RBF) kernels that determine how input points affect each other (Chen and Ser, 2009). This renders it an optimal solution in scenarios where data scarcity or high observation costs prevail, such as in GNSS campaign measurements. However, as with high-rate GNSS observations, when data volumes increase significantly, processing large data sets creates a serious computational burden and complicates the practical application of the method. Due to increased programming requirements and processing costs, traditional applications lose their applicability when dealing with large and high-dimensional data sets (Liu *et al.*, 2020; Roushangar and Shahnazi, 2020). The GPR model can be expressed as:

$$SL(t) \sim GP[m(t),\ k(t,t')] \tag{5}$$

where $m(t)$ is the mean function representing the expected value at time t, and $k(t,t')$ is the covariance function (kernel) that expresses the relationship between the values at times t and t'.

2.3.4. Criteria used in interpreting results

In addition to the traditional linear model, three criteria, such as R^2, *MAE* and *RMSE* (Table 2), are very important in interpreting the results obtained through ML procedures such as RF, DT, and GPR.

Table 2 - Criteria used in interpreting the results and mathematical models

R^2	• Indicates how well the model explains the variance in the dependent variable. • Commonly used to evaluate model accuracy in GNSS velocity prediction.	$R^2 = 1 - \frac{\sum_i^n (y_i - \hat{y}_i)^2}{\sum_i^n (y_i - \bar{y}_i)^2}$
MAE	• Measures the average magnitude of prediction errors, regardless of direction. • Less sensitive to outliers, useful for general model accuracy.	$MAE = \frac{1}{n}\sum_{i=1}^n \lvert y_i - \hat{y}_i \rvert$
RMSE	• Indicates the square root of the average squared prediction errors. • More sensitive to large errors, useful when large deviations matter.	$RMSE = \sqrt{\frac{1}{n}\sum_{i=1}^n (y_i - \hat{y}_i)^2}$

2.3.5. Model training and hyperparameter optimisation

All models were trained and evaluated using the MATLAB R2023a Statistics and machine learning toolbox. To ensure the reliability of GNSS velocity estimation with ML approaches, the model training and evaluation process was followed. In order to evaluate the model performance, the dataset was divided into 80% training and 20% testing. For model validation and hyperparameter tuning, five-fold cross-validation was applied. This ensured both robustness and minimised overfitting. Early stopping was not applied, but overfitting was monitored by comparing training and validation performance with *MAE* and *RMSE* metrics. The observation time (epoch) and the north and east components of the GNSS stations in the Gauss-Krueger projection were selected as model inputs.

These features were determined in order to capture the spatial and temporal changes of the models. In the model training phase, each model was trained with different techniques for hyperparameter optimisation:

The DT model is optimised using Grid Search with tree depth and minimum leaf node size; RF is evaluated with different numbers of trees, between 100 and 500, to find the best configuration; GPR is optimised using the RBF kernel and hyperparameters are cross-validated. The trained models were measured using three different criteria, such as R^2, *MAE*, and *RMSE*, with the help of 20% test data. The findings indicate that DT and RF models show the highest level of accuracy for CORS data and are effective in capturing nonlinear trends in continuous GNSS time series. In the context of campaign-based GNSS observations, GPR has been shown to outperform other methods. This can be attributed to the probabilistic nature of the model and its capacity to more effectively generalise with limited data.

3. Results and discussions

When the data for all stations are analysed, the R^2 values obtained from the CORSs are greater than 94% for four models (0.99985-0.94081). *MAE* values vary between 0.50 mm and 6.37 mm. On the other hand, *RMSE* values vary between 0.64 mm and 3.95 mm (Table 3). The models with the largest R^2 values are RF and DT, while the *RMSE* values are the smallest. These values give similar results for both horizontal components. On the other hand, in the campaign data, the largest values of R^2 are GPR and LR, while *RMSE* values are the smallest. However, in RF and DT methods, *RMSE* values reach up to 40.53 mm and good results cannot be obtained. When Table 3 is examined, for the CORS observations, the metrics determined from all methods (velocity, R^2, *MAE*, and *RMSE*) are close to each other (in agreement with published data). It is known that the method with the highest R^2 value and the smallest *MAE* and *RMSE* gives the best results. In this case, while the best results are obtained from the DT method in almost all of the data, the results of the RF method are more suitable in the eastern component of the KUN0 and TGBU stations.

In addition, to provide a statistical visual interpretation of the model performances, box plots (Fig. 3) for *MAE* values and violin plots (Fig. 4) for *RMSE* values were drawn using the results presented in Table 3.

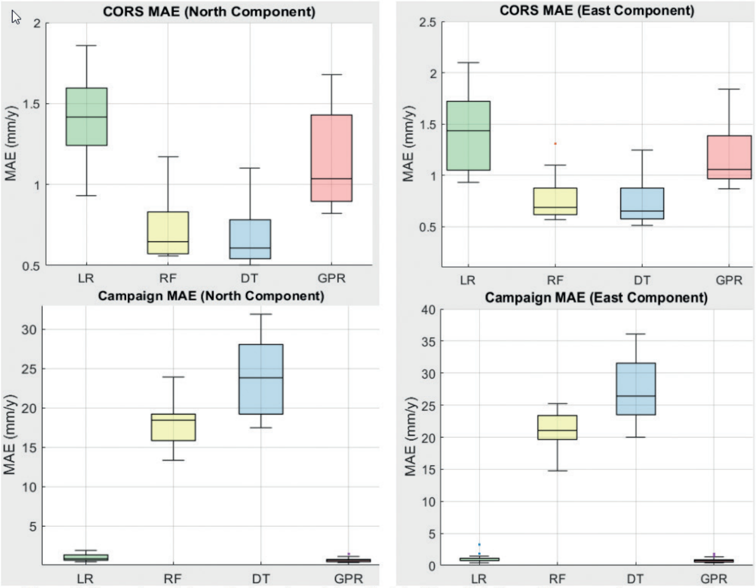

Fig. 3 - Box plot graphs based on data calculated for all stations. These graphs compare the distribution of the prediction performance of different ML models. The height of the box indicates the data spread, while the median line indicates the centre position. Wide boxes indicate greater variability in errors, while narrow boxes indicate greater consistency in models. In this respect, the box plot is a quick and effective comparison tool.

Table 3 - Calculated velocity and other statistical metrics of the horizontal components of the stations.

			CORS observations				**Campaign measurements**			
St. ID	**Comp.**	**Model**	**Vel. (mm/y)**	**R^2**	***MAE* (mm/y)**	***RMSE* (mm/y)**	**Vel. (mm/y)**	**R^2**	***MAE* (mm/y)**	***RMSE* (mm/y)**
0LOD	**North**	**LR**	14.9	0.99836	1.09	1.85	14.5	0.99959	1.55	1.78
		RF	14.9	0.99966	0.60	0.83	12.3	0.93964	16.62	21.53
		DT	14.9	0.99977	0.55	0.70	13.6	0.93761	18.96	21.89
		GPR	14.9	0.99898	0.90	1.45	14.5	0.99987	0.66	0.98
	East	**LR**	18.3	0.99898	1.44	1.78	18.8	0.99989	0.92	1.17
		RF	18.3	0.99979	0.64	0.82	16.3	0.94695	20.41	26.20
		DT	18.3	0.99980	0.62	0.78	17.6	0.93763	24.49	28.41
		GPR	18.3	0.99950	0.99	1.25	18.8	0.99993	0.77	0.94
0SKL	**North**	**LR**	14.2	0.99888	1.42	1.80	14.4	0.99990	0.65	0.83
		RF	14.2	0.99969	0.73	0.94	12.3	0.93554	16.39	21.14
		DT	14.2	0.99974	0.68	0.87	13.6	0.93865	17.53	20.63
		GPR	14.2	0.99940	1.03	1.32	14.4	0.99995	0.48	0.57
	East	**LR**	19.2	0.99916	1.71	2.11	18.9	0.99985	1.07	1.36
		RF	19.2	0.99983	0.75	0.95	16.1	0.93311	23.08	28.21
		DT	19.2	0.99983	0.75	0.94	17.8	0.94039	22.73	26.63
		GPR	19.2	0.99967	1.04	1.31	18.9	0.99993	0.74	0.92
0SKN	**North**	**LR**	14.9	0.99826	1.52	1.92	14.2	0.99967	1.29	1.57
		RF	14.9	0.99975	0.57	0.73	12.5	0.94870	15.35	19.47
		DT	14.9	0.99977	0.55	0.70	13.3	0.93932	18.26	21.17
		GPR	14.9	0.99940	0.89	1.13	14.2	0.99977	1.05	1.30
	East	**LR**	18.4	0.99910	1.30	1.70	19.1	0.99987	1.11	1.30
		RF	18.4	0.99982	0.60	0.76	16.3	0.93819	23.01	28.69
		DT	18.4	0.99982	0.60	0.76	17.9	0.93942	24.31	28.41
		GPR	18.4	0.99962	0.87	1.11	19.1	0.99988	1.04	1.26
BUDP	**North**	**LR**	15.0	0.99792	1.55	3.55	14.3	0.99992	0.60	0.83
		RF	15.0	0.99906	0.86	2.40	12.7	0.95764	13.95	18.65
		DT	15.0	0.99981	0.82	1.07	13.4	0.93683	19.71	22.77
		GPR	15.0	0.99794	1.53	3.54	14.3	0.99996	0.50	0.60
	East	**LR**	18.0	0.99948	1.38	2.12	18.5	0.99995	0.62	0.80
		RF	18.0	0.99976	0.90	1.44	16.2	0.95284	19.75	25.53
		DT	18.0	0.99984	0.91	1.16	17.4	0.93830	25.30	29.21
		GPR	18.0	0.9995	1.34	2.08	18.5	0.99998	0.44	0.56
GESR	**North**	**LR**	15.2	0.99721	1.64	3.75	16	0.99990	0.71	0.93
		RF	15.2	0.99874	0.82	2.52	13.6	0.93303	19.01	23.87
		DT	15.2	0.99981	0.75	0.99	15	0.93883	19.40	22.81
		GPR	15.2	0.99728	1.57	3.70	16	0.99995	0.56	0.68
	East	**LR**	18.4	0.99916	1.65	2.49	18	0.99977	1.34	1.59
		RF	18.4	0.99971	0.86	1.47	14.9	0.92065	23.33	29.28
		DT	18.4	0.99983	0.86	1.11	17	0.94114	21.44	25.22
		GPR	18.4	0.99931	1.43	2.26	18	0.99994	0.57	0.79

Table 3 - continued.

			CORS observations				**Campaign measurements**			
St. ID	**Comp.**	**Model**	**Vel. (mm/y)**	R^2	***MAE* (mm/y)**	***RMSE* (mm/y)**	**Vel. (mm/y)**	R^2	***MAE* (mm/y)**	***RMSE* (mm/y)**
HOL2	**North**	**LR**	15.6	0.99826	1.46	1.93	15.8	0.99972	1.06	1.44
		RF	15.6	0.99948	0.75	1.06	13.0	0.91604	20.44	25.05
		DT	15.6	0.99957	0.69	0.96	13.6	0.85965	26.68	32.39
		GPR	15.6	0.99899	1.07	1.48	15.8	0.99987	0.74	0.98
	East	**LR**	17.6	0.99867	1.43	1.90	17.8	0.99985	0.98	1.20
		RF	17.6	0.99965	0.71	0.98	14.8	0.92499	21.31	26.76
		DT	17.6	0.99970	0.66	0.90	15.3	0.85770	30.23	36.85
		GPR	17.6	0.99922	1.08	1.46	17.8	0.99994	0.64	0.77
SAS2	**North**	**LR**	15.4	0.99667	1.23	1.55	14.9	0.99941	0.80	0.93
		RF	15.4	0.99889	0.68	0.89	13.6	0.84865	23.94	29.46
		DT	15.4	0.99914	0.59	0.79	14.2	0.75972	31.86	37.12
		GPR	15.4	0.99758	1.04	1.32	14.9	0.99967	0.63	0.70
	East	**LR**	19.3	0.99791	1.23	1.54	19.3	0.99949	1.04	1.13
		RF	19.3	0.99934	0.67	0.87	10.1	0.84244	18.09	22.61
		DT	19.3	0.99949	0.58	0.76	10.6	0.74888	24.52	28.54
		GPR	19.3	0.99866	0.96	1.23	19.3	0.99981	0.55	0.69
TGBU	**North**	**LR**	16.4	0.99863	1.84	2.25	16.4	0.99948	1.37	1.73
		RF	16.4	0.99982	0.63	0.81	12.8	0.87807	22.42	26.40
		DT	16.4	0.99983	0.62	0.80	12.4	0.76466	31.94	36.67
		GPR	16.4	0.99966	0.88	1.11	16.4	0.99973	0.84	1.25
	East	**LR**	17.4	0.99727	2.83	3.36	17.5	0.99947	1.46	1.86
		RF	17.4	0.99980	0.70	0.90	13.5	0.87227	23.98	28.83
		DT	17.4	0.99980	0.72	0.91	13.1	0.74760	35.58	40.53
		GPR	17.4	0.99934	1.31	1.65	17.5	0.99955	1.32	1.71
TGDA	**North**	**LR**	15.4	0.99923	1.25	1.58	15.7	0.99959	1.13	1.46
		RF	15.4	0.99978	0.66	0.84	11.8	0.86667	21.19	26.40
		DT	15.4	0.99979	0.65	0.82	11.8	0.74507	31.69	36.50
		GPR	15.4	0.99939	1.11	1.41	15.7	0.99993	0.47	0.60
	East	**LR**	16.4	0.98503	6.37	7.50	16.1	0.99906	1.84	2.27
		RF	16.4	0.99957	0.98	1.28	12.3	0.87992	20.91	25.68
		DT	16.4	0.99959	0.96	1.24	12.2	0.76601	31.27	35.85
		GPR	16.4	0.98548	6.25	7.38	16.1	0.99949	1.45	1.68
WARN	**North**	**LR**	15.3	0.99657	1.86	3.98	14.8	0.99952	1.78	2.05
		RF	15.3	0.99856	0.84	2.58	12.9	0.95145	15.58	20.66
		DT	15.3	0.99907	0.81	2.07	13.8	0.93513	20.63	23.89
		GPR	15.3	0.99733	1.28	3.51	14.8	0.99967	1.48	1.70
	East	**LR**	18.6	0.99922	1.47	2.30	19.6	0.99987	1.13	1.40
		RF	18.6	0.99969	0.83	1.45	17.4	0.95822	19.53	25.39
		DT	18.6	0.99984	0.82	1.05	18.4	0.93852	26.68	30.80
		GPR	18.6	0.99944	1.13	1.94	19.6	0.99993	0.85	1.06

Table 3 - continued.

			CORS observations				Campaign measurements			
St. ID	**Comp.**	**Model**	**Vel. (mm/y)**	***R*²**	***MAE* (mm/y)**	***RMSE* (mm/y)**	**Vel. (mm/y)**	***R*²**	***MAE* (mm/y)**	***RMSE* (mm/y)**
0VAR	**North**	**LR**	15.0	0.99874	1.33	1.68	14.1	0.99949	0.89	1.29
		RF	15.0	0.99974	0.60	0.76	10.0	0.83547	18.67	22.99
		DT	15.0	0.99977	0.57	0.73	10.6	0.75236	24.08	28.21
		GPR	15.0	0.99942	0.90	1.14	14.1	0.99975	0.76	0.89
	East	**LR**	17.6	0.99791	2.10	2.55	18.4	0.99963	1.13	1.43
		RF	17.6	0.99977	0.65	0.84	13.3	0.84725	23.51	28.95
		DT	17.6	0.99978	0.65	0.83	13.8	0.75229	31.73	36.86
		GPR	17.6	0.99940	1.09	1.37	18.4	0.99971	0.97	1.26
0YST	**North**	**LR**	14.8	0.99783	1.64	1.99	14.4	0.99967	0.87	1.06
		RF	14.8	0.99970	0.58	0.74	10.1	0.83879	18.35	23.30
		DT	14.8	0.99975	0.53	0.67	10.8	0.75143	24.83	28.94
		GPR	14.8	0.99788	1.63	1.96	14.4	0.99988	0.52	0.64
	East	**LR**	18.3	0.99947	0.97	1.21	18.7	0.99993	0.46	0.65
		RF	18.3	0.99979	0.59	0.76	13.0	0.84247	23.94	29.87
		DT	18.3	0.99981	0.57	0.72	14.1	0.75306	32.08	37.40
		GPR	18.3	0.99950	0.94	1.18	18.7	0.99995	0.41	0.55
1BAG	**North**	**LR**	15.2	0.99786	1.31	1.61	14.2	0.99972	0.69	0.83
		RF	15.2	0.99955	0.57	0.74	10.2	0.85126	15.03	18.94
		DT	15.2	0.99965	0.50	0.65	10.7	0.75425	21.25	24.34
		GPR	15.2	0.99910	0.82	1.04	14.2	0.99977	0.65	0.74
	East	**LR**	16.9	0.99889	1.03	1.28	18.2	0.99951	1.11	1.39
		RF	16.9	0.99958	0.61	0.79	12.0	0.83166	19.66	25.82
		DT	16.9	0.99967	0.54	0.70	13.8	0.75936	27.06	30.87
		GPR	16.9	0.99897	0.99	1.24	18.2	0.99974	0.73	1.02
ESBC	**North**	**LR**	15.5	0.99796	1.41	1.78	15.3	0.99992	0.52	0.78
		RF	15.5	0.99900	0.97	1.25	12.7	0.92672	18.65	23.84
		DT	15.5	0.99925	0.81	1.08	14.4	0.93987	18.36	21.59
		GPR	15.5	0.99798	1.40	1.77	15.3	0.99996	0.45	0.57
	East	**LR**	17.5	0.99759	1.74	2.20	17.3	0.99993	0.65	0.83
		RF	17.5	0.99898	1.10	1.43	14.7	0.93676	19.90	25.15
		DT	17.5	0.99920	0.97	1.27	16.3	0.94129	20.66	24.24
		GPR	17.5	0.99774	1.67	2.13	17.3	0.99995	0.55	0.68
FER5	**North**	**LR**	15.3	0.99013	1.05	3.95	15.1	0.99975	0.84	1.10
		RF	15.3	0.99303	0.65	3.32	11.5	0.87723	19.47	24.34
		DT	15.3	0.99973	0.52	0.66	11.3	0.74667	30.44	34.96
		GPR	15.3	0.99021	1.02	3.94	15.1	0.99994	0.45	0.54
	East	**LR**	16.6	0.94081	1.25	10.78	17.0	0.99986	0.76	0.91
		RF	16.6	0.95802	0.87	9.08	12.8	0.87199	23.37	28.00
		DT	16.6	0.99977	0.53	0.68	12.8	0.75308	34.25	38.89
		GPR	16.6	0.94081	1.26	10.78	17.0	0.99988	0.77	0.86

Table 3 - continued.

			CORS observations				**Campaign measurements**			
St. ID	**Comp.**	**Model**	**Vel. (mm/y)**	R^2	***MAE* (mm/y)**	***RMSE* (mm/y)**	**Vel. (mm/y)**	R^2	***MAE* (mm/y)**	***RMSE* (mm/y)**
FYHA	**North**	**LR**	15.5	0.99889	0.98	1.22	15.6	0.99979	0.57	0.79
		RF	15.5	0.99961	0.56	0.72	10.6	0.84333	16.17	21.31
		DT	15.5	0.99969	0.50	0.64	11.7	0.74898	23.64	26.97
		GPR	15.5	0.99902	0.92	1.15	15.6	0.99994	0.37	0.43
	East	**LR**	17.6	0.99908	1.00	1.27	17.6	0.99993	0.45	0.51
		RF	17.6	0.99966	0.60	0.77	11.8	0.84162	18.37	24.13
		DT	17.6	0.99973	0.53	0.68	13.3	0.75555	26.25	29.97
		GPR	17.6	0.99922	0.93	1.17	17.6	0.99993	0.45	0.51
HIRS	**North**	**LR**	15.1	0.99780	1.48	1.87	15.6	0.99968	1.35	1.62
		RF	15.1	0.99892	1.01	1.31	13.3	0.93210	18.99	23.40
		DT	15.1	0.99925	0.84	1.10	14.6	0.93894	18.81	22.19
		GPR	15.1	0.99785	1.46	1.85	15.6	0.99993	0.61	0.75
	East	**LR**	16.9	0.99768	1.70	2.15	16.7	0.99977	1.17	1.45
		RF	16.9	0.99905	1.06	1.38	13.8	0.92813	20.33	25.80
		DT	16.9	0.99930	0.89	1.18	15.7	0.94070	19.95	23.43
		GPR	16.9	0.99781	1.64	2.09	16.7	0.99986	0.85	1.12
KUN0	**North**	**LR**	14.9	0.99904	1.26	1.55	15.0	0.99920	1.94	2.45
		RF	14.9	0.99979	0.57	0.73	12.6	0.92991	17.90	22.97
		DT	14.9	0.99980	0.56	0.72	13.1	0.86937	26.14	31.36
		GPR	14.9	0.99942	0.96	1.20	15.0	0.99970	1.16	1.50
	East	**LR**	19.0	0.99966	0.93	1.18	19.0	0.99904	3.26	3.39
		RF	19.0	0.99985	0.62	0.79	15.7	0.93646	21.25	27.62
		DT	19.0	0.99984	0.62	0.80	17.9	0.94222	22.67	26.34
		GPR	19.0	0.99970	0.88	1.11	19.0	0.99957	1.80	2.27
ONSA	**North**	**LR**	14.7	0.99914	1.70	2.24	15.4	0.99994	0.71	1.02
		RF	14.7	0.99959	1.17	1.56	14.4	0.97994	13.34	18.31
		DT	14.7	0.99964	1.10	1.46	14.5	0.93649	28.09	32.57
		GPR	14.7	0.99916	1.68	2.22	15.4	0.99994	0.71	1.02
	East	**LR**	17.3	0.99922	1.90	2.51	16.6	0.99995	0.82	0.98
		RF	17.3	0.99962	1.31	1.75	15.5	0.97972	14.71	19.74
		DT	17.3	0.99967	1.25	1.63	15.5	0.93821	29.71	34.47
		GPR	17.3	0.99926	1.84	2.45	16.6	0.99996	0.78	0.90
TEJH	**North**	**LR**	15.0	0.99719	0.95	1.19	14.8	0.99969	0.91	1.14
		RF	15.0	0.99892	0.57	0.74	10.4	0.85575	18.84	24.33
		DT	15.0	0.99916	0.50	0.65	11.1	0.74399	28.09	32.41
		GPR	15.0	0.99780	0.83	1.06	14.8	0.99971	0.92	1.09
	East	**LR**	18.4	0.99781	1.02	1.29	18.9	0.99979	0.91	1.19
		RF	18.4	0.99898	0.67	0.88	13.9	0.85471	25.28	31.18
		DT	18.4	0.99926	0.57	0.75	14.1	0.74379	36.09	41.41
		GPR	18.4	0.99791	0.99	1.26	18.9	0.99990	0.63	0.82

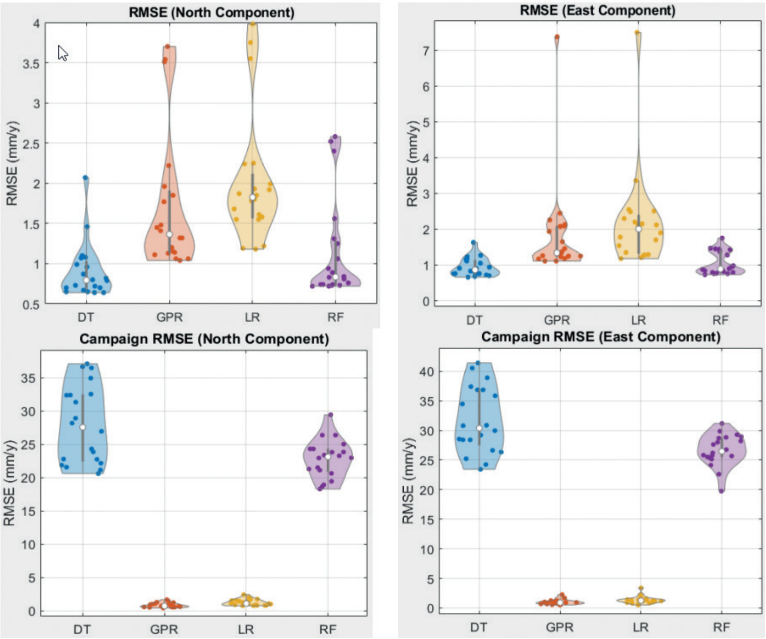

Fig. 4 - Violin plots make it easy to compare the distribution shape and density of data. Similar to box plots, they show statistics such as the median, quartiles, and outliers, while also reflecting the distribution density of the data. Wide areas in the graph indicate that the data are denser in that value range, while narrow areas indicate that the data are sparse. The median value, typically shown as a white dot on the violin plot, represents the central position of the data.

The metrics obtained show significant deviations when RF and DT methods are used, especially in datasets characterised by sparse distribution, such as campaign data. Tree-based models stand out for their ability to process large datasets. They typically require a significant amount of data volume to prevent overfitting, especially in cases of limited or noisy observations.

In contrast, linear models such as LR and advanced models such as GPR have shown a higher degree of fit with smaller datasets, especially when the data exhibit smooth or continuous trends. Among all the data belonging to the campaign measurements, the best results were obtained with the GPR method, which can be explained by the limited dataset of the campaign data. LR operates under the assumption of linear relationships and can, therefore, effectively model simpler relationships in the data without overcomplicating the underlying structure (Schoukens *et al.*, 2017). GPR offers a distinct advantage by using a probabilistic approach that incorporates uncertainty directly into predictions through the use of kernel functions. This makes GPR particularly effective at capturing trends, even in the presence of sparse data or measurement uncertainty (Kierulf *et al.*, 2012; Bishnoi *et al.*, 2019). Findings from GPR application demonstrate the agreement between predictions and actual ground motion patterns in data-scarce contexts, thus highlighting the ability of such applications to facilitate precise and true interpolation of missing information (Bogusz *et al.*, 2019). However, there are exceptions at the stations. Nevertheless, the LR method yielded better results with the exception of the eastern component at the FYHA station and the northern component at the ONSA station. It is evaluated that these deviations in both the KUN0 and TGBU stations in the CORS observation and campaign measurement data at the FYHA and ONSA stations are due to geographical conditions.

Erkoç and Doğan (2024) compared the linear model and Support Vector Machines learning approach while determining the sea level trends in Shikoku Island of Japan and reached more accurate results while determining trends with the ML approach. In another study, Siemuri *et al.* (2022) presented a systematic review of ML techniques for prediction of GNSS data and highlighted their potential to improve the accuracy of analysis results. Arabi *et al.* (2023) found that the integration of hybrid models, such as CNN-LSTM architecture, shows promise in improving the accuracy of GNSS-derived measurements. Li *et al.* (2023) modelled GNSS velocities with ML methods such as GBDT and XGBoost and obtained better results than the least squares fitting methods. Crocetti *et al.* (2021) emphasised the importance of reliably identifying discontinuities to improve the robustness of velocity estimates derived from GNSS data and found that the RF approach yielded better results. In the present study, in addition to other studies, the GNSS time series of 20 stations were analysed and the velocities of GNSS stations were segmented. The DT approach for the CORSs and the GPR approach for campaign-based data showed the best performance. This difference is thought to be due to the fact that CORS data (daily solution) are affected by annual and semiannual seasonal effects, while campaign-type data are not affected by these effects and linearise more quickly since they are made in the same month every year.

Southern Scandinavia is a region where major tectonic deformations are relatively rare, but where crustal movements caused by coastal erosion are experienced. Coastal systems are one of the most dynamic structures on Earth and are constantly changing at various spatial-temporal scales (Ranasinghe, 2016). Shoreline change, sediment loading, and sea level changes can cause regional crustal deformation (Almar *et al.*, 2021).

Updated GNSS velocities in the ITRF2020 reference frame allow for a more detailed assessment of ongoing movements in the region. The ML approaches used in this study detected the details of velocity changes at high resolution. In particular, DT and RF algorithms successfully captured nonlinear patterns in GNSS velocity time series, allowing for a better understanding of regional crustal movements. These results reveal that existing geophysical models in the region need to be further improved.

On the other hand, there are velocity data published by institutions and organisations such as JPL, Université de la Rochelle (ULR), Geo Forschungs Zentrum (GFZ), and Nevada Geodetic Laboratory (NGL) (SONEL, n.d.) (Table 4).

Table 4 shows that the velocities published by GFZ and JPL cover a very limited number of stations. The velocity data published by NGL covers all stations, while the data published by ULR is missing only for stations SAS2 and FER5. Therefore, the deviation (%) values between the NGL and ULR data and the velocities within this range were calculated (Fig. 5). On average, the deviation between the velocities calculated from the CORS data and the published velocity data is 1.32 and 0.93 for the northern component as published by ULR and NGL, respectively, and 1.07 and 1.03 for the eastern component. Thus, the data agree with each other.

This confirms the robustness of the velocity estimates in the present study and shows that there are significant differences at some stations. Compared to previous studies, significant differences were observed especially at the KUN0 and TGBU stations. It is considered that these differences may be due to reasons such as station location, environmental effects, and seasonal changes. The calculated velocities contribute to a more precise evaluation of the crustal movements in the region.

On the other hand, there are data of some of the selected stations from which horizontal GNSS velocities of the study area were calculated. Altamimi *et al.* (2012) computed the GNSS velocities of the stations used in the study as WARN, SAS2, and BUDP. In another study, Altamimi *et al.* (2023) calculated the velocities of 10 GNSS stations (0LOD, 0SKL, 0SKN, BUDP, HOL2, SAS2, WARN, 0YST, FYHA, TEJH) in the current study. The Pearson correlation coefficient was calculated for the velocities (radial) found for these stations and two datasets were compared. The result was a correlation coefficient of 0.89, showing a strong relationship between the two sets of data. This shows that the datasets are very compatible.

However, this study has systematically compared the performance of classical LR models and modern ML algorithms in estimating GNSS velocities, also showing some limitations. It might

Table 4 - Published horizontal velocities of the stations used in the study and publishing organisations.

Station ID	**Component**	**Institutions and organisations publishing the data**			
		ULR	**GFZ**	**NGL**	**JPL**
0LOD	North	14.83 ± 0.08	-	14.87 ± 0.12	-
	East	18.12 ± 0.10	-	18.36 ± 0.15	-
0SKL	North	14.81 ± 0.08	-	14.68 ± 0.13	-
	East	18.36 ± 0.04	-	18.43 ± 0.12	-
0SKN	North	15.07 ± 0.07	-	14.83 ± 0.12	-
	East	18.01 ± 0.05	-	18.10 ± 0.12	-
BUDP	North	15.02 ± 0.06	14.38 ± 0.10	15.10 ± 0.11	15.07 ± 0.04
	East	18.14 ± 0.06	18.75 ± 0.10	18.09 ± 0.11	18.06 ± 0.03
GESR	North	15.08 ± 0.07	15.91 ± 0.10	15.20 ± 0.12	-
	East	18.47 ± 0.06	17.72 ± 0.10	18.32 ± 0.12	-
HOL2	North	15.36 ± 0.06	15.50 ± 0.10	15.21 ± 0.14	-
	East	17.92 ± 0.04	17.90 ± 0.10	18.14 ± 0.14	-
SAS2	North	-	-	15.55 ± 0.26	-
	East	-	-	19.15 ± 0.28	-
TGBU	North	15.61 ± 0.15	-	15.68 ± 0.16	-
	East	17.28 ± 0.22	-	17.71 ± 0.20	-
TGDA	North	15.62 ± 0.14	-	15.55 ± 0.15	-
	East	16.93 ± 0.86	-	16.50 ± 0.36	-
WARN	North	15.64 ± 0.10	14.67 ± 0.10	15.51 ± 0.14	15.44 ± 0.05
	East	18.60 ± 0.08	19.02 ± 0.10	18.79 ± 0.12	18.75 ± 0.03
0VAR	North	14.63 ± 0.07	-	14.90 ± 0.16	-
	East	17.38 ± 0.15	-	17.69 ± 0.18	-
0YST	North	14.86 ± 0.06	-	14.95 ± 0.14	-
	East	18.26 ± 0.04	-	18.47 ± 0.14	-
1BAG	North	15.04 ± 0.07	-	15.14 ± 0.17	-
	East	16.86 ± 0.08	-	16.98 ± 0.20	-
ESBC	North	15.43 ± 0.06	15.42 ± 0.10	15.40 ± 0.12	-
	East	17.41 ± 0.07	17.44 ± 0.10	17.25 ± 0.14	-
FER5	North	-	-	15.47 ± 0.15	-
	East	-	-	16.70 ± 0.17	-
FYHA	North	15.44 ± 0.08	-	15.54 ± 0.15	-
	East	17.63 ± 0.09	-	17.76 ± 0.17	-
HIRS	North	15.14 ± 0.07	15.86 ± 0.10	15.32 ± 0.12	-
	East	16.80 ± 0.06	15.62 ± 0.10	16.64 ± 0.12	-
KUN0	North	14.41 ± 0.06	-	14.52 ± 0.14	-
	East	18.50 ± 0.12	-	18.84 ± 0.13	-
ONSA	North	14.79 ± 0.07	15.40 ± 0.10	14.84 ± 0.11	14.81 ± 0.03
	East	17.30 ± 0.08	16.50 ± 0.10	17.22 ± 0.12	17.20 ± 0.02
TEJH	North	15.02 ± 0.11	-	15.16 ± 0.16	-
	East	18.43 ± 0.07	-	18.92 ± 0.17	-

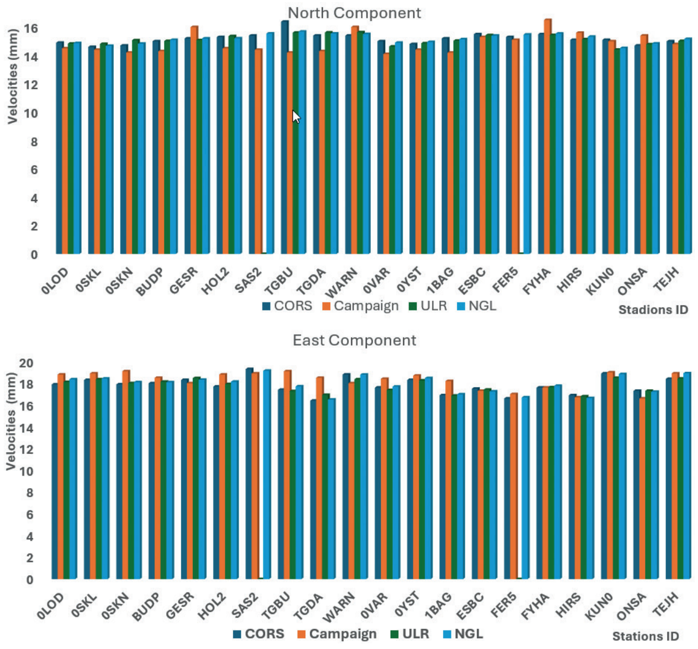

Fig. 5 - Station velocities calculated from CORS and campaign measurements within the scope of the study, along with velocities published by ULR and NGL.

not represent the entire study area because the distribution of 20 GNSS stations may be very spotty in regions with sparse station coverage. Data gaps, although dealt with by interpolation, could affect the reliability of the results. Moreover, the annual and semi-annual effects may not be captured by the campaign data GNSS measurements used in this study, which could affect velocity estimates from continuous GNSS observations. GPR, in particular, has computational costs that will limit its ability to be used on larger datasets. Additionally, the study area is tectonically stable and does not provide insight to the model's performance in dynamic regions.

Fig.6 shows the velocities of the stations in the study area. The Leba Ridge-Riga-Pskov Fault Zone (LRRP FZ) is located in the eastern part of the study area. The fact that the station velocities in the eastern part of the study area are relatively larger than those in the western

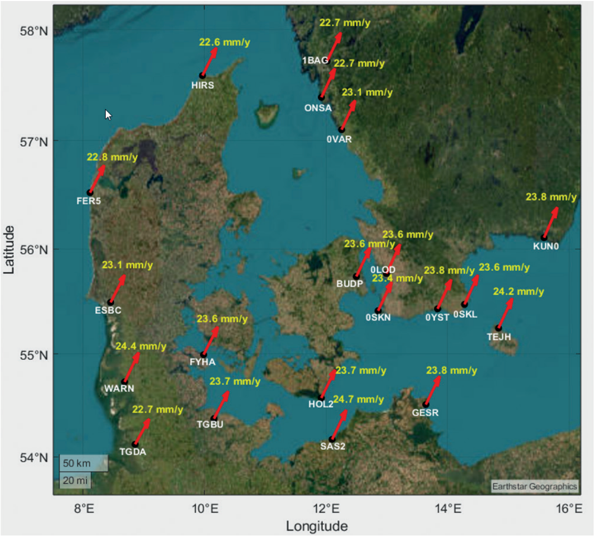

Fig. 6 - Velocity map based on the velocities published by NGL.

part may be due to the influence of this fault. However, the lack of empirical evidence prevents the verification of these claims. It is hypothesised that old tectonic zones, such as the LRRP FZ, may have exerted an influence on regional deformation patterns due to the redistribution of stress across the Fennoscandian Shield by means of the glacial isostatic adjustment processes. Despite the absence of a direct signal in the estimated velocities, subsequent studies may prove beneficial in investigating the potential correlation between these small GNSS velocity trends at the eastern stations and the fault systems within the Baltic transition zone.

Finally, while long-term trends in velocity were well analysed, the capability of these models regarding the capture of short-term deformation remains untested. These limitations show some avenues for future research and underline the cautious interpretation that the findings deserve.

4. Conclusions

In this study, we investigated the performance of different ML approaches with a LR model to determine the horizontal velocities of 20 GNSS stations. The R^2 values calculated for CORS data showed a very high accuracy above 0.94. Furthermore, the MAE ranged from 0.50 mm to 6.37 mm, while the $RMSE$ ranged from 0.64 mm to 10.78 mm. Therefore, when MAE and $RMSE$ values, which are other criteria of accuracy, are considered together with R^2, RF and DT give better results.

In the campaign measurement data, GPR and LR methods performed better, showing the highest R^2 and lowest $RMSE$ values. However, $RMSE$ values for RF and DT in the campaign data reached up to 40.53 mm at certain stations and were considered to be due to geographical conditions. The comparison of the results with velocity data published by organisations like NGL and ULR shows very good compatibility, with a deviation of 1.32% for the north component and 1.07% for the east component. It is shown that ML approaches outperform the traditional methods in GNSS velocity estimation and point out the influence of seasonal effects in CORS data modelling.

It is evaluated that the use of ML techniques contributes to the understanding of crustal deformation in southern Scandinavia by providing precise rate estimates. Future research is recommended to integrate this approach with geophysical models to develop new strategies for more precise prediction of long-term crustal change.

Acknowledgments. We would like to thank all data providers. GNSS data was obtained from SONEL. The velocity data of the stations were obtained from the data archive published by ULR, JPL, GFZ and NGL.

REFERENCES

Agarwal K., Ainapure B. and Shukla A.; 2023: *A comprehensive review of the GNSS with IoT applications and their use cases with special emphasis on Machine Learning and Deep Learning Models.* Int. J. Recent Innovation Trends Comput. Commun., 11, 220-230, doi: 10.17762/ijritcc.v11i10s.7622.

Alif S.M., Siagian J.M., and Anggara O.; 2023: *Present-day crustal deformation in west Sumatra after series of Sumatran great earthquake from 2004-2010. J. Earth Mar. Tech. (JEMT)*, 3, 59-68, doi: 10.31284/j.jemt.2023.v3i2.3733

Almar R., Ranasinghe R., Bergsma E.W.J., Diaz H., Melet A., Papa F., Vousdoukas M., Athanasiou P., Dada O., Almeida L.P. and Kestenare E.; 2021: *A global analysis of extreme coastal water levels with implications for potential coastal overtopping.* Nat. Commun., 12, 3775, doi: 10.1038/s41467-021-24008-9.

Altamimi Z., Métivier L. and Collilieux X.; 2012: *ITRF2008 plate motion model.* J. Geophys. Res.: Solid Earth, 117, doi: 10.1029/2011JB008930.

Altamimi Z., Rebischung P., Métivier L., and Collilieux X.; 2016: *ITRF2014: a new release of the International Terrestrial Reference Frame modeling nonlinear station motions*. J. Geophys. Res.: Solid Earth, 121, 6109-6131, doi: 10.1002/2016JB013098.

Altamimi Z., Métivier L., Rebischung P., Collilieux X., Chanard K. and Barnéoud J.; 2023: *ITRF2020 plate motion model.* Geophys. Res. Lett., 50, e2023GL106373, doi: 10.1029/2023GL106373.

Angrisano A., Cappello G., Gaglione S. and Gioia C.; 2024: *Velocity estimation using time-differenced carrier phase and doppler shift with different grades of devices: from smartphones to professional receivers.* Algorithms, 17, doi: 10.3390/a17010002.

Arabi S., Asgarimehr M., Kada M. and Wickert J.; 2023: *Hybrid CNN-LSTM deep learning for track-wise GNSS-R ocean wind speed retrieval.* Remote Sens., 15, 4169, doi: 10.3390/rs15174169.

Atia M.M., Noureldin A. and Korenberg M.; 2011: *Gaussian process regression approach for bridging GPS outages in integrated navigation systems.* Electron. Lett., 47, 52-53, doi: 10.1049/el.2010.7164.

Bishnoi S., Singh S., Ravinder R., Bauchy M., Gosvami N.N., Kodamana H. and Krishnan N.; 2019: *Predicting Young's modulus of oxide glasses with sparse datasets using machine learning.* J. Non-Cryst. Solids, 524, 119643, doi: 10.1016/j.jnoncrysol.2019.119643

Bogusz J., Kłos A. and Pokonieczny K.; 2019: *Optimal strategy of a GPS position time series analysis for post-glacial rebound investigation in europe.* Remote Sens., 11, 1209, doi: 10.3390/rs11101209.

Chen H. and Ser W.; 2009: *Sound source DOA estimation and localization in noisy reverberant environments using least-squares support vector machines.* J. Signal Process. Syst., 63, 287-300, doi: 10.1007/s11265-009-0423-7.

Christianti D., Abdullah S. and Nurrohmah S.; 2020: *Bayes risk post-pruning in decision tree to overcome overfitting problem on customer churn classification*. In: Proc. 1st International Conference on Statistics and Analytics, ICSA 2019, Bogor, Indonesia, doi: 10.4108/eai.2-8-2019.2290487.

Crocetti L., Schartner M. and Soja B.; 2021: *Discontinuity detection in GNSS station coordinate time series using Machine Learning.* Remote Sens., 13, 3906, doi: 10.3390/rs13193906.

Dalmasso M., Civera M., De Biagi V. and Chiaia B.; 2025: *Gaussian Process Regression (GPR)-based missing data imputation and its uses for bridge structural health monitoring.* ABEN, 6, 23, doi: 10.1186/s43251-025-00169-1.

Dittmann T., Liu Y., Morton Y. and Mencin D.; 2022: *Supervised Machine Learning of high rate GNSS velocities for earthquake strong motion signals.* J. Geophys. Res.: Solid Earth., 127, e2022JB024854, doi: 10.1029/2022JB024854.

Erkoç M.H. and Doğan U.; 2023: *Datum definition for geodetic vertical velocity field derived from GNSS observations: a case study in western and southern Turkey.* Bull. Geoph. Ocean., 64, 135-148, doi: 10.4430/bgo00412.

Erkoç M.H. and Doğan U.; 2024: *Machine Learning models applied to altimetry era tide gauge and grid altimetry data for comparative long-term trend estimation: a study from Shikoku Island, Japan.* Appl. Ocean Res., 150, 104132, doi: 10.1016/j.apor.2024.104132.

Gao W., Li Z., Chen Q., Jiang W. and Feng Y.; 2022: *Modelling and prediction of GNSS time series using GBDT, LSTM and SVM machine learning approaches.* J. Geod., 96, doi: 10.1007/s00190-022-01662-5.

Granat R., Donnellan A., Heflin M., Lyzenga G., Glasscoe M., Parker J., Pierce M., Wang J., Rundle J. and Ludwig L.G.; 2021: *Clustering analysis methods for GNSS observations: a data-driven approach to identifying California's major faults*. Earth Space Sci., 8, e2021EA001680, doi: 10.1029/2021EA001680.

Heflin M., Donnellan A., Parker J., Lyzenga G., Moore A., Ludwig L.G., Rundle J., Wang J. and Pierce M.; 2020: *Automated estimation and tools to extract positions, velocities, breaks, and seasonal terms from daily GNSS measurements: illuminating nonlinear Salton trough deformation.* Earth Space Sci., 7, e2019EA000644, doi: 10.1029/2019EA000644.

Hewing L., Kabzan J. and Zeilinger M.N.; 2019: *Cautious model predictive control using Gaussian Process Regression.* IEEE Trans. Control Syst. Technol., 28, 2736-2743, doi: 10.1109/tcst.2019.2949757.

Kamatham Y.; 2018: *Prediction of multipath interference for static GNSS applications.* CVR J. Sci. Technol., 14, doi: 10.32377/cvrjst140.

Kierulf H., Ouassou M., Simpson M. and Vestøl O.; 2012: *A continuous velocity field for Norway*. J. Geod., 87, 337-349, doi: 10.1007/s00190-012-0603-2.

Kim S., Ree J.H., Yoon H.S., Choi B.K. and Park P.H.; 2018: *Crustal deformation of South Korea after the Tohoku-Oki earthquake: deformation heterogeneity and seismic activity*. Tectonics, 37, 2389-2403, doi: 10.1029/2018tc004967.

Li Z., Lu T., Yu K. and Wang J.; 2023: *Interpolation of GNSS position time series using GBDT, XGBoost, and RF machine learning algorithms and models error analysis*. Remote Sens., 15, 4374, doi: 10.3390/rs15184374.

Marotta A. and Sabadini R.; 2002: *Tectonic versus glacial isostatic deformation in Europe.* Geophys. Res. Lett., 29, doi: 10.1029/2001gl013865.

Okazaki T., Fukahata Y. and Nishimura T.; 2021: *Consistent estimation of strain-rate fields from GNSS velocity data using basis function expansion with ABIC*. Earth, Planets Space, 73, doi: 10.1186/s40623-021-01474-5.

Peng D., Feng L., Larson K.M. and Hill E.M.; 2021: *Measuring coastal absolute sea-level changes using GNSS interferometric reflectometry*. Remote Sens., 13, 4319, doi: 10.3390/rs13214319.

Qiang B., Shi K., Liu N., Zhao P. and Ren J.; 2023: *Application of cutting power consumption in tool condition monitoring and wear prediction based on Gaussian process regression under variable cutting parameters.* Int. J. Adv. Manuf. Technol., 124, doi: 10.1007/s00170-022-10459-x.

Quan Y., Lau L., Roberts G.W., Meng X. and Zhang C.; 2018: *Convolutional neural network based multipath detection method for static and kinematic GPS high precision positioning*. Remote Sens., 10, 2052, doi: 10.3390/rs10122052.

Ranasinghe R.; 2016: *Assessing climate change impacts on open sandy coasts: a review*. *Earth Sci. Rev.,* 160, 320-332, doi: 10.1016/j.earscirev.2016.07.011.

Roushangar K. and Shahnazi S.; 2020: *Prediction of sediment transport rates in gravel-bed rivers using Gaussian process regression.* J. Hydroinf., 22, 249-262, doi: 10.2166/hydro.2019.077.

Schoukens M., Hammenecker J. and Cooman A.; 2017: *Obtaining the preinverse of a power amplifier using iterative learning control.* Ieee Transactions on Microwave Theory and Techniques, 65(11), 4266-4273, doi: 10.1109/tmtt.2017.2694822.

Siemuri A., Selvan K., Kuusniemi H., Valisuo P. and Elmusrati M.S.; 2022: *A systematic review of Machine Learning techniques for GNSS use cases.* IEEE Trans. Aerosp. Electron. Syst., 58, 5043-5077, doi: 10.1109/TAES.2022.3219366.

SONEL; n.d.: *GNSS.* https://www.sonel.org/-GPS-.html?lang=en, accessed November 2024.

Sośnica K., Bury G. and Zajdel R.; 2018: *Contribution of multi-GNSS constellation to SLR-derived terrestrial reference frame.* Geophys. Res. Lett., 45, 2339-2348, doi: 10.1002/2017GL076850.

USGS, n.d.: *Earthquake Hazards Program.* https://www.usgs.gov/programs/earthquake-hazards, accessed November 2024.

Vu N.Q., Le T.N. and Luong N.D.; 2023: *Analysis of bridge displacement using GNSS time-series data*. IOP Conference Series: Mater. Sci. Eng., 1289, 012034, doi: 10.1088/1757-899x/1289/1/012034.

Wang S., Li J., Chen J. and Hu X.; 2022: *On the improvement of mass load inversion with GNSS horizontal deformation: a synthetic study in central China.* J. Geophys. Res.: Solid Earth, 127(10), doi: 10.1029/2021jb023696.

Yáñez-Cuadra V., Moreno M., Ortega-Culaciati F., Donoso F., Báez J.C. and Tassara A.; 2023: *Mosaicking Andean morphostructure and seismic cycle crustal deformation patterns using GNSS velocities and Machine Learning.* Front. Earth Sci., 11, 1096238, doi: 10.3389/feart.2023.1096238.

Zhang Y. and Wang L.; 2019: *A hybrid intelligent algorithm DGP-MLP for GNSS/INS integration during GNSS outages*. J. Navig., 72, doi: 10.1017/S0373463318000760.

Zhang Z., Zhang H. and Shi Y.; 2025: *Reconciling high-resolution strain rate of continental China from GNSS data with the spherical spline interpolation.* Tectonophys., 898, 230614, doi: 10.1016/j.tecto.2024.230614.

Corresponding author: Mehmet Eren
Yildiz Technical University, Department of Geomatic Engineering
34220 Istanbul, Türkiye
Tel: +90 212 383 5203; e-mail: meren@yildiz.edu.tr